Supporting Information

Rice Leaves Microstructures Inspired High-Efficiency Electrodes for Green Hydrogen Production

Yuliang Li[a]†, Jinxin Gao[a]†, Zhaoyang Wang[a], Honghao Li[a], Lu Li[a], Xiaofang Zhang[b]*, Xiaoyang Fan[a], Longyun Lin[a], Yan Li[c], Ke Li[a], Chunyu Zhang[a], Linyang Li[a], Ran Wang[a], Yunting Su[a], and Dongliang Tian[a]*

[a]Key Laboratory of Bio-Inspired Smart Interfacial Science and Technology, School of Chemistry, Beihang University, Beijing 100191, P. R. China

[b]School of Mathematics and Physics, University of Science & Technology Beijing, Beijing 100083, P. R. China

[c]State Key Laboratory of Nonlinear Mechanics, Beijing Key Laboratory of Engineered Construction and Mechanobiology, Institute of Mechanics, Chinese Academy of Sciences, Beijing 100190, P. R. China

*Correspondence E-mail: tiandl@buaa.edu.cn; xfzhang926@ustb.edu.cn

†These authors contributed equally to this work.

Electrochemical measurements

Electrochemical tests were conducted in 1.0 M KOH electrolyte with an electrochemical analyzer (model CHI660E, CH Instruments). The fabricated electrodes served as the working electrode (dimensioned at 1 cm × 1 cm), Hg/HgO as a reference electrode ($E^{\Theta}_{\mathrm{Hg/HgO}}$ = 0.098 V vs. SHE) and counter electrode as a graphite rod. The hydrogen evolution reaction (HER) and oxygen evolution reaction (OER) polarization curves were characterized at scanning rates of 5 $\mathrm{mV\cdot s^{-1}}$ in selected potential ranges, and all polarization curves were performed with *iR* compensation. The electrolyte was bubbled with O_2 (OER) or Ar (HER) for at least 30 min. All potentials were calibrated to the reversible hydrogen electrode (RHE) according to the following Eq. S1:

$$E_{\mathrm{RHE}} = E_{\mathrm{Hg/HgO}} + 0.059\ \mathrm{pH} + 0.098\ \mathrm{V} \qquad \text{(Eq. S1)}$$

Electrochemical impedance spectroscopy (EIS) was measured with an AC voltage with 5 mV amplitude in the frequency range from 0.01 Hz to 100 kHz. The electrolyte resistance was obtained by the fitted Nyquist plots, and this value was used for *iR* compensation using the following equation: [1]

$$E_{\mathrm{iR-corrected}} = E_{original} - IR_s \qquad \text{(Eq. S2)}$$

The overall water splitting efficiency was measured in two-electrode system utilizing the prepared electrodes as both cathode and anode. LSV curves were obtained at a scan rate of 5 $\mathrm{mV\cdot s^{-1}}$. Stability measurements were performed at potential of -0.09 V vs. RHE for 30 h (HER) and 1.35 V vs. RHE for 30 h (OER). Bubble size distributions were observed in chronopotentiometry mode at a current density of 10 $\mathrm{mA\cdot cm^{-2}}$. As the comparison samples, 5 mg of RuO_2 and 20 wt% Pt/C were ultrasonically dispersed in a mixture of 500 μL of ethanol, 450 μL of deionized water, and 50 μL of 5% Nafion, and the dispersion was transferred to on groove Ni metal and flat Ni metal for electrochemical measurement.

Electrochemical surface area (ECSA)

ECSA values were obtained from the cyclic voltammetry (CV) curves of the electrodes at different scanning rates in the non-Faraday region (**Fig. S18**). The CV curve was used to evaluate the electrochemical double layer capacitance (C_{dl}) at different scanning rates: 5, 10, 15, 20, 25 mV·s^{-1}. We used a specific capacitance of 40 μF·cm^{-2} (20-60 μF·cm^{-2}) to calculate the ECSA according to Eq. S3: [2, 3]

$$\mathrm{ECSA} = \frac{C_{\mathrm{dl}}}{40\ \mu\mathrm{F\ cm}^{-2}}\ cm^2_{\mathrm{ECSA}} \qquad (\mathrm{Eq.\,S3})$$

Faraday efficiency (FE)

Faraday efficiency is calculated by comparing the volume of gas experimentally (V_{a}) produced by the prepared electrodes with the volume of gas calculated theoretically (V_{b}):

$$\mathrm{FE} = \frac{V_a}{V_b} \qquad (\mathrm{Eq.\,S4})$$

The experimental volume of H_2/O_2 is determined by draining water. The theoretical volume can be found by the Eq. S5:

$$V_b = \frac{i\ t\ V_m}{n_e\ F} \qquad (\mathrm{Eq.\,S5})$$

Where t is the electrolysis time and V_{m} (24.5 L·mol^{-1}, 298 K, 101 kPa) is the molar volume of H_2/O_2,[4] and n_e is the number of electrons required for one molecule of H_2/O_2.

Bubble driving force (F_{d}) and contact angle hysteresis (F_{CAH})

The driving force of bubble movement (F_{d}) is the component of buoyancy force along the groove direction (Y-direction):

$$F_{\mathrm{d}} = \rho V g \sin\alpha \qquad (\mathrm{Eq.\,S6})$$

where g, ρ, V and α denote the gravitational acceleration, water density, volume of the bubble and the inclination angle of the surface, respectively. As indicated by Eq. 6, the computed force F_{d} is determined to be 6.82×10^{-5} N using **Table S1**, corresponding to the movement of 50 μL bubble along the surface of the Ni-conductive in the Y direction at an angle of 8°.

Resistance to the bubble movement along the groove direction is the contact angle hysteresis (F_{CAH}): [5]

$$F_{\mathrm{CAH}} = \gamma L(\cos\theta_r - \cos\theta_{\mathrm{a}}) \qquad (\mathrm{Eq.\,S7})$$

where γ, L, θ_{r} and θ_{a} represent the water surface tension, length of three phase contact line, receding and advancing angles of the bubble, respectively. In contrast, the resistance to the bubble's progression in the same direction is due to the contact angle hysteresis force, F_{CAH}. Upon a 50 μL bubble gliding along 8° inclined Ni-conductive surface in the Y-direction, the main sliding resistance of bubbles is the F_{CAH} of bubbles is 6.6×10^{-5} N. Perpendicular to the groove (X-direction), the F_{CAH} is greater than F_{d} (with a value of 18.2×10^{-5} N exceeding 6.82×10^{-5} N), impeding the bubble's slide at nearly an 8° incline. However, when in the Y direction, the F_{CAH} is less than F_{d} (6.6×10^{-5} N compared to 6.82×10^{-5} N), facilitating the bubble's movement along the groove. For a Ni-smooth surface with an identical inclination, the F_{d} for a 50 μL bubble in either direction is less than the F_{CAH} (with a value of 25.5×10^{-5} N), resulting in the bubble's inability to move.

Computational fluid dynamics (CFD) simulation Study

Simulations were carried out using ANSYS Fluent software, the electrode and gas basin were modeled using computer-aided design software, and after meshing by Fluent Meshing, the pressure-based solver was applied for steady state solution. The wall is set as a no-slip stationary wall, the inlet is a velocity inlet with an inlet velocity of 0.01 $\mathrm{m \cdot s^{-1}}$, and the outlet is a pressure outlet with a gauge pressure of 0 Pa. The laminar flow model is applied to perform the calculations to solve the mass conservation equation (continuity equation) and momentum conservation equation (N-S equation).

Mass conservation equation:

$$\frac{\partial \rho}{\partial t} + \frac{\partial (\rho u)}{\partial x} + \frac{\partial (\rho v)}{\partial y} + \frac{\partial (\rho w)}{\partial z} = 0 \qquad \text{(Eq. S8)}$$

where ρ is the fluid density, t is the time, and u, v, and w are the velocity vectors along the x, y, and z directions, respectively.

Conservation of momentum equation:

$$\frac{\partial (\rho u_i)}{\partial t} + \frac{\partial \left(\rho u_i u_j\right)}{\partial x_j} = -\frac{\partial p}{\partial x_i} + \frac{\partial \tau_{ij}}{\partial x_j} + \rho g_i \qquad \text{(Eq. S9)}$$

where p is the static pressure, τ_{ij} is the stress tensor, and g_i is the gravitational volumetric force in the i direction. The initial position of droplets or bubbles is set by cell marking and local initialization, the surface tension coefficient between liquid and gas is 0.07 $\mathrm{N \cdot m^{-1}}$, and the gravitational acceleration in the y-direction is -9.81 $\mathrm{m \cdot s^{-2}}$.

The solution is carried out by using the VOF multiphase flow model and laminar model, and in addition to the equations of conservation of mass (continuity equations), and momentum (N-S equations), the equations of volume fraction are also required to be solved.

Volume fraction equation:

For the q-th phase, the equation has the following form:

$$\frac{1}{\rho_q}\left[\frac{\partial}{\partial t}\left(\alpha_q \rho_q\right) + \nabla \cdot \left(\alpha_q \rho_q \overrightarrow{v_q}\right)\right] = \sum_{p=1}^{n}\left(\dot{m_{pq}} - \dot{m_{qp}}\right) \qquad (\mathrm{Eq.\,S10})$$

where $\dot{m_{qp}}$ is the mass transferred from the q-phase to the p-phase; $\dot{m_{pq}}$ is the mass transferred from the p-phase to the q-phase. α_q is the volume fraction of the q-phase, and ρ_q is the density of the q-phase.

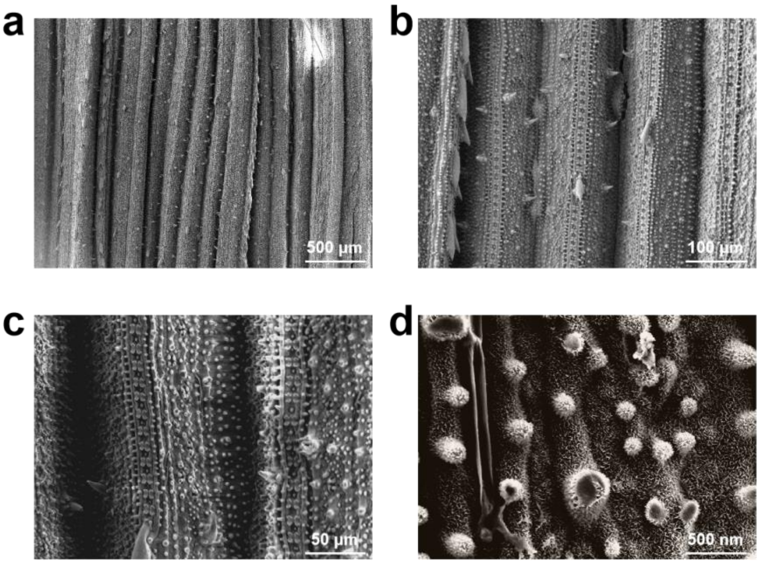

Fig. S1 SEM images of rice leaves at different scales: (a) 500 μm, (b) 100 μm, (c) 50 μm, and (d) 500 nm.

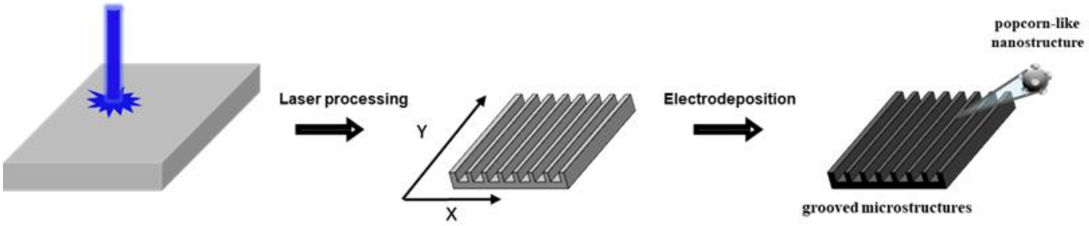

Fig. S2 Preparation diagram of anisotropic microstructured gas conduction electrode (Ni-conduction) by laser and electrodeposition.

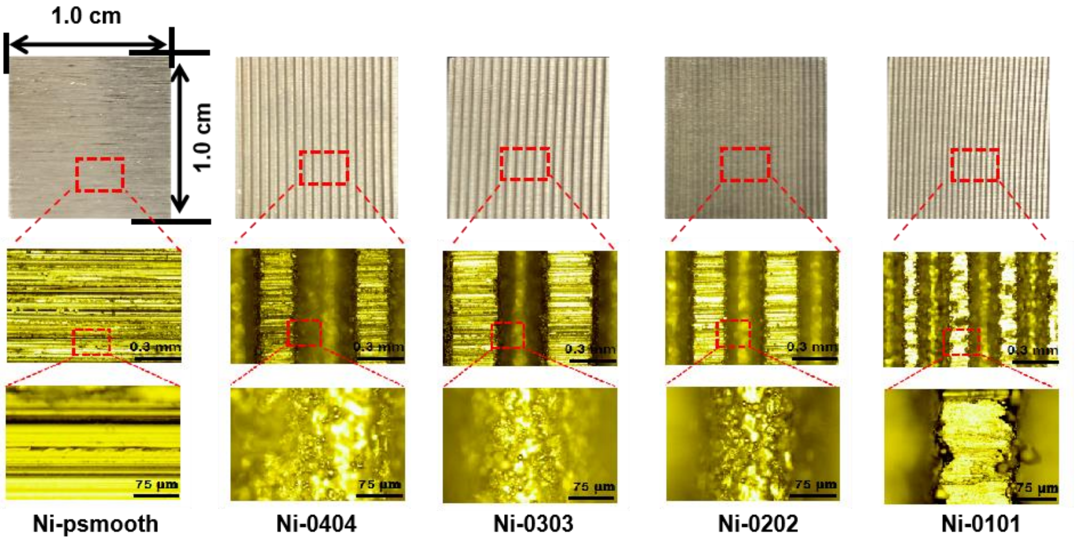

Fig. S3 Different microscope photographs of flat Ni metal, Ni-0404 (groove width: 0.4 mm; spacing width: 0.4 mm), Ni-0303 (groove width: 0.3 mm; spacing width: 0.3 mm), Ni-0202 (groove width: 0.2 mm; spacing width: 0.2 mm), and Ni-0101 (groove width: 0.1 mm; spacing width: 0.1 mm) were prepared by laser etching.

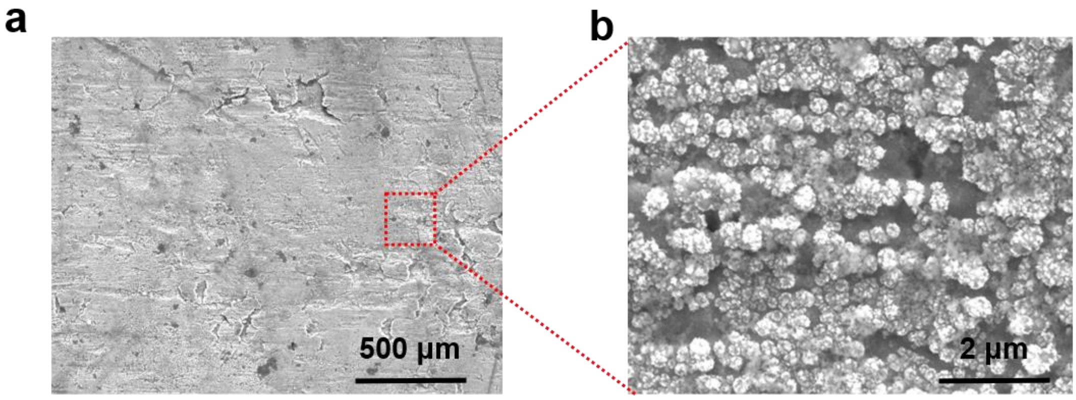

Fig. S4 SEM images of Ni-smooth at low magnifications (a) and high magnifications (b).

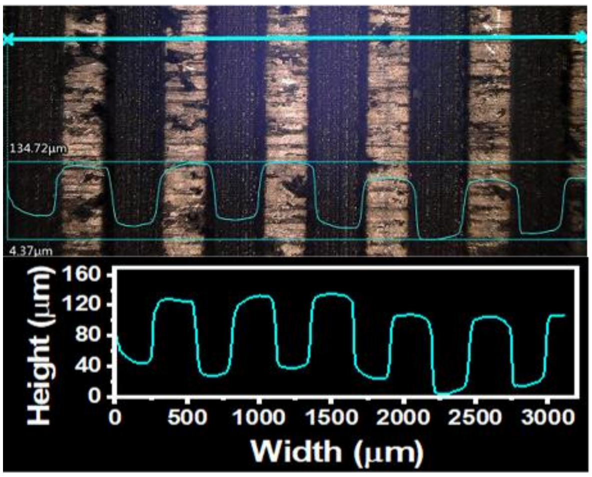

Fig. S5 Three-dimensional microscope image of Ni-conduction.

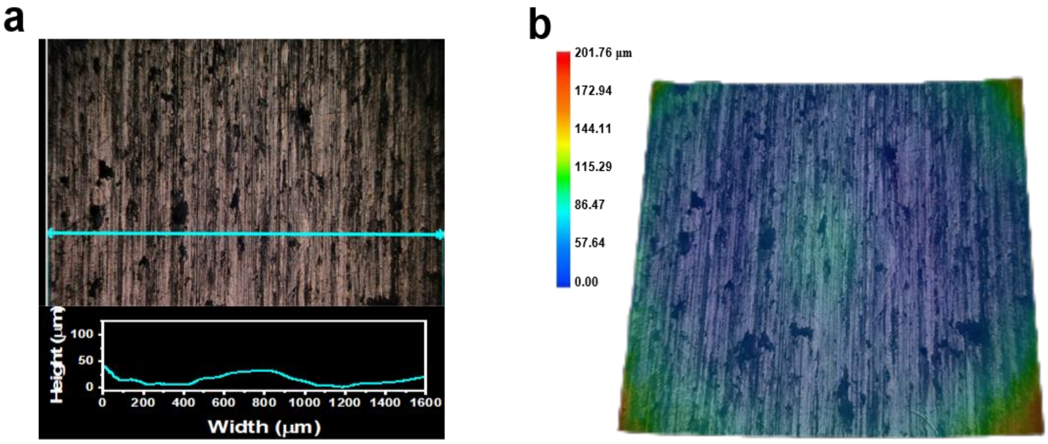

Fig. S6 (a) Three-dimensional microscope image of Ni-smooth. (b) Three-dimensional simulation of the Ni-smooth.

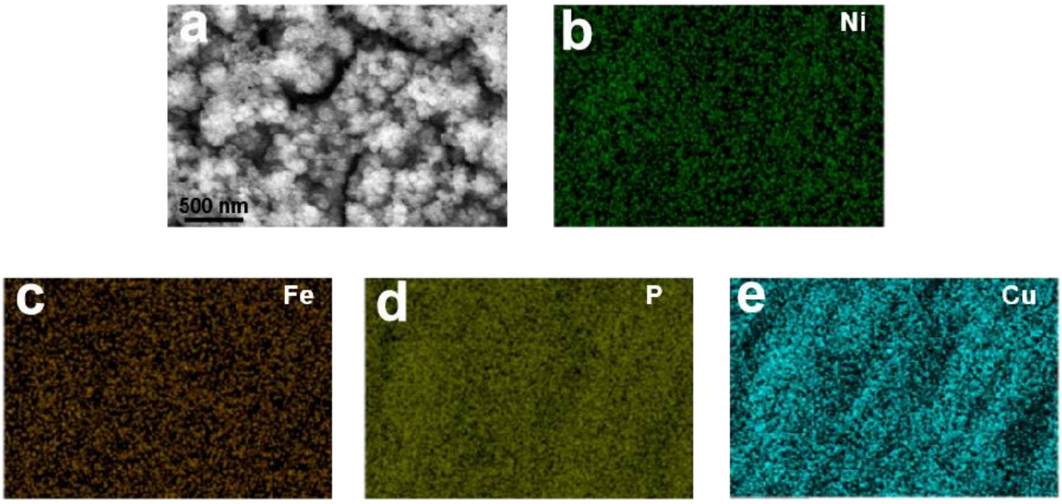

Fig. S7 SEM and EDS mapping images of electrodeposition synthesized NiFeCuP layer. SEM image (a), (b-e) EDS mapping images of Ni, Fe, P, and Cu, respectively.

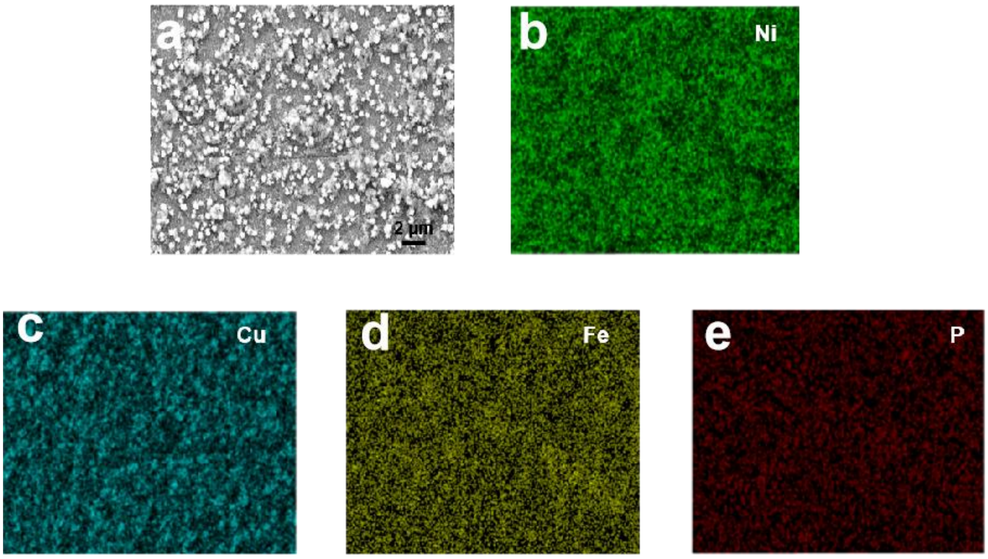

Fig. S8 SEM and EDS mapping images of flat nickel electrode (Ni-smooth). SEM image (a), (b-e) EDS mapping images of Ni, Cu, Fe, and P, respectively.

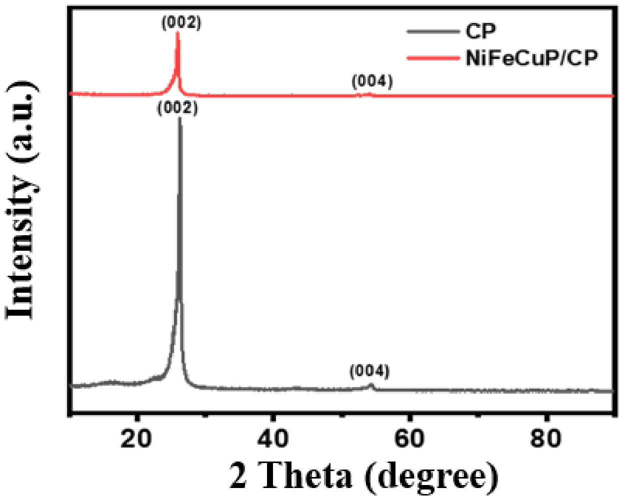

Fig. S9 XRD patterns of carbon paper (CP) and NiFeCuP/CP.

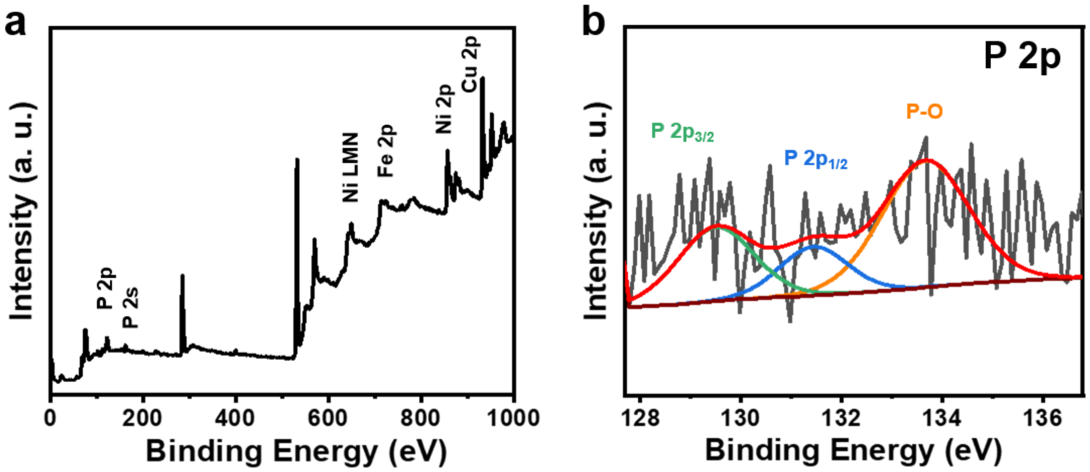

Fig. S10 XPS survey result of Ni-conduction (a) and high-resolution XPS spectra of P 2p (b) for Ni-conduction.

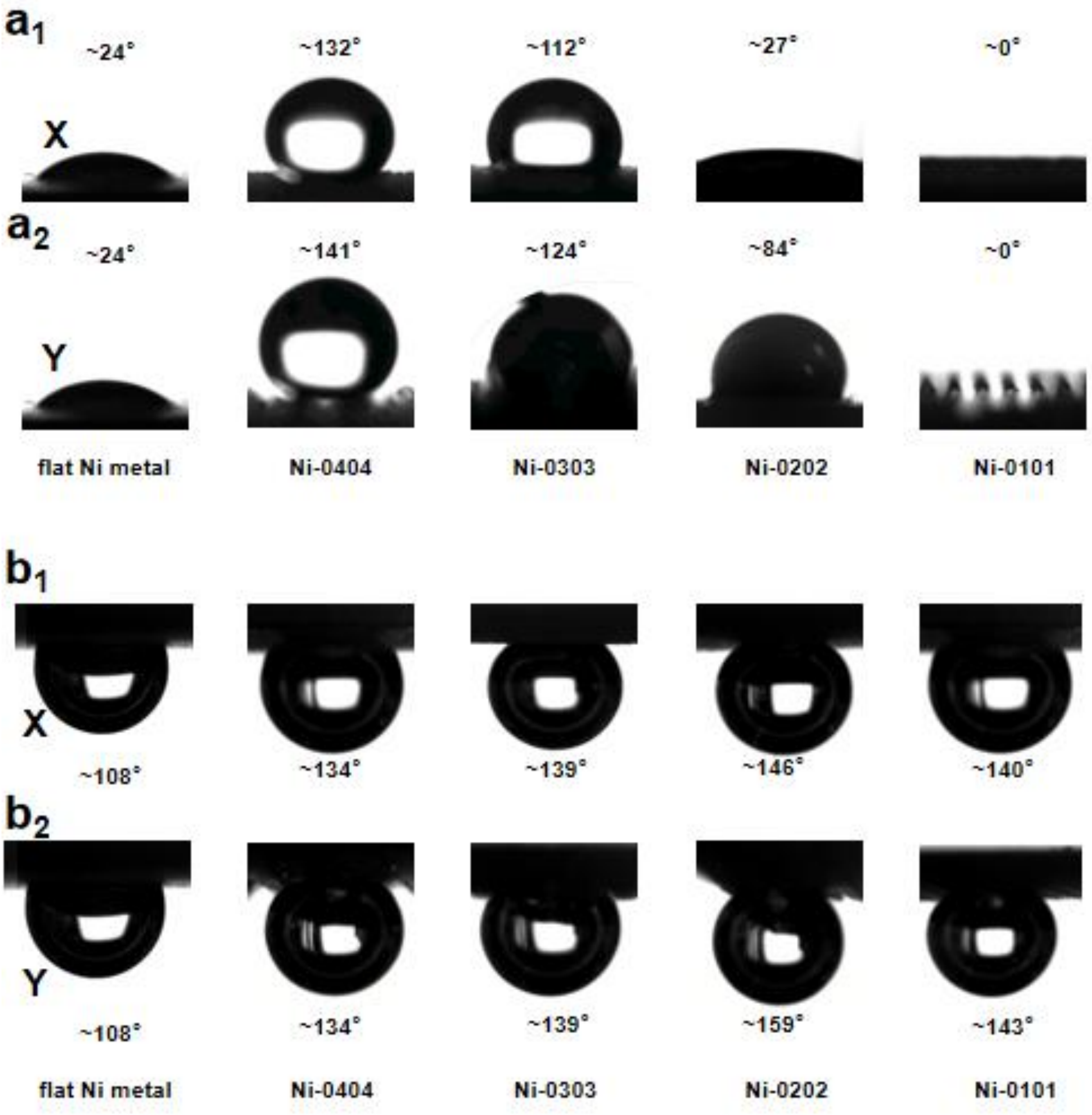

Fig. S11 The wettability of bubbles and liquid droplets with different morphologies was named along the groove direction in X-direction and perpendicular groove direction in Y-direction. Water droplet (5 μL) contact angle in X-direction (a_1) and Y-direction (a_2) with different morphologies. Bubble (5 μL) contact angle in X-direction (b_1) and Y-direction (b_2) of different morphologies.

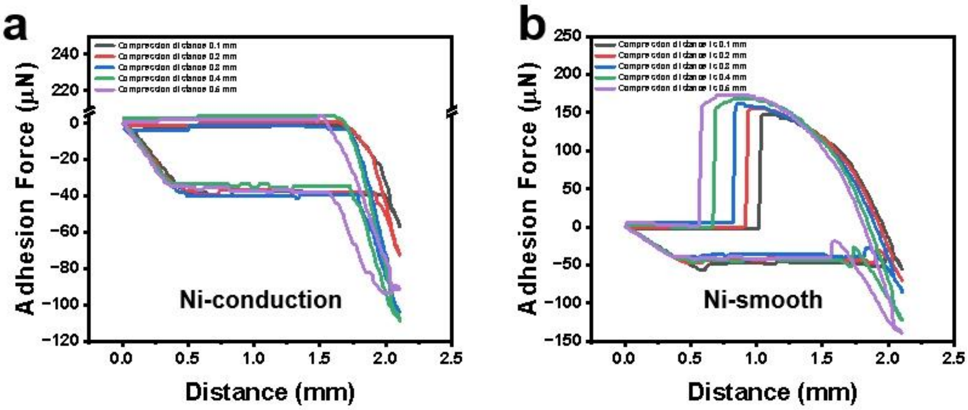

Fig. S12 The bubble (5 μL) adhesion force test on the surface of Ni-conduction (a) and Ni-smooth (b) at different compression distances.

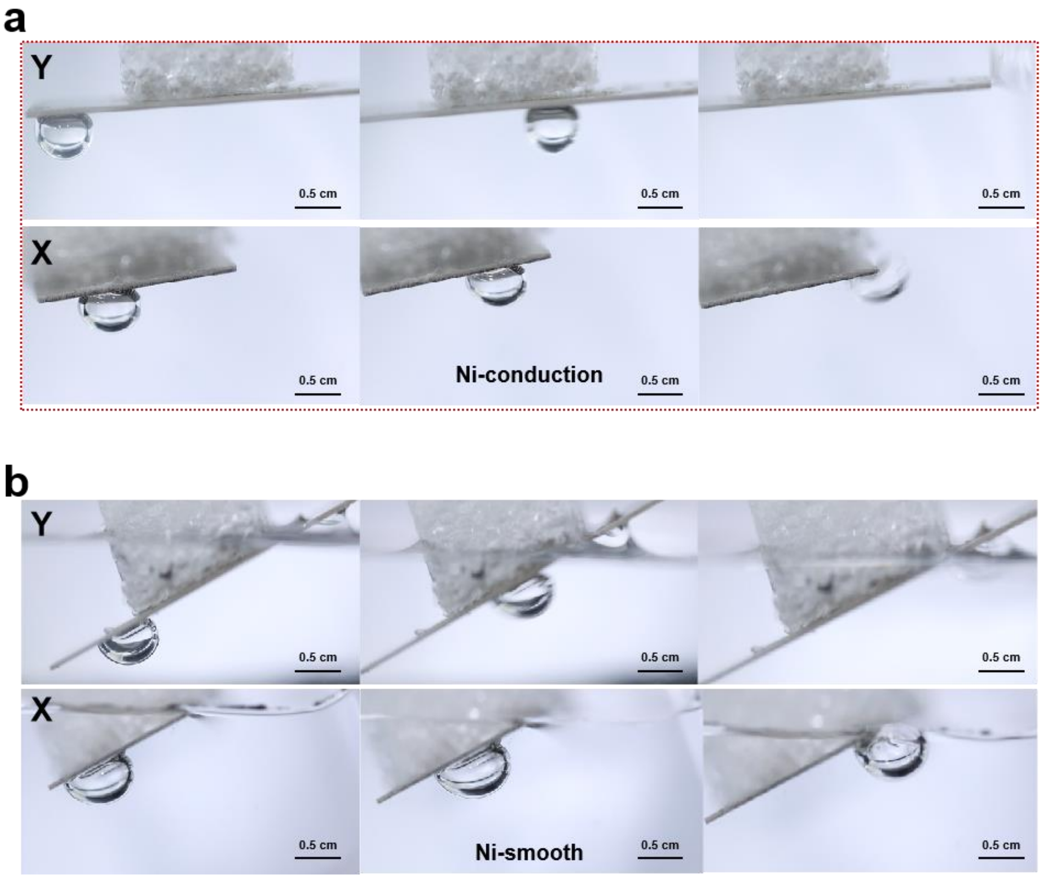

Fig. S13 (a) When the 10 μL bubble rolls on the Ni-conduction, the bubble sliding angle in Y-direction is 8° and in X-direction is 24°. (b) When a 10 μL bubble rolls on Ni-smooth, its sliding angle is 31° in the Y-direction and 31° in the X-direction.

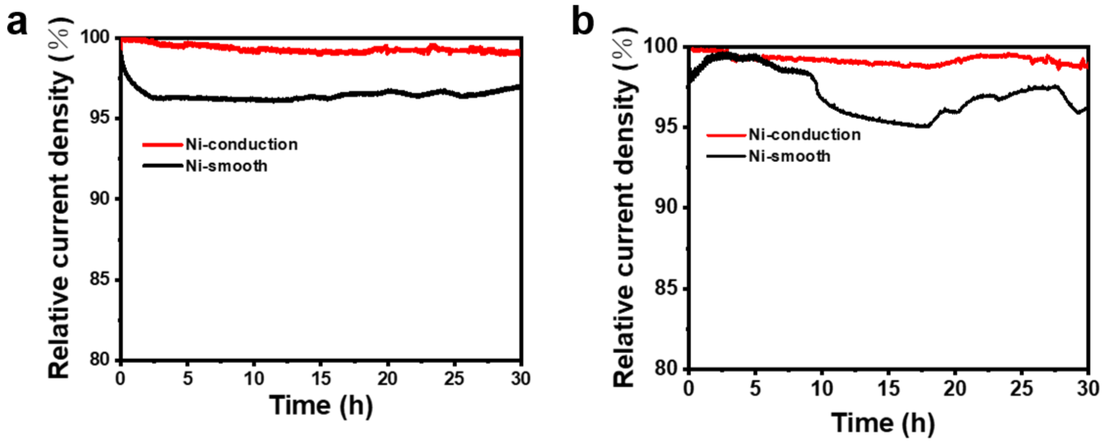

Fig. S14 The HER (a) and OER (b) chronoamperometry curves of Ni-conduction and Ni-smooth electrodes for 30 h.

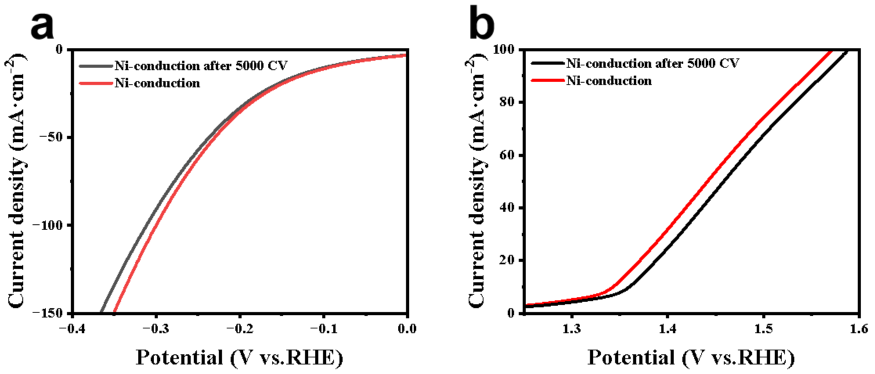

Fig. S15 After 5000 CV cycle, the LSV curve of Ni-conduction electrode for HER (a) and OER (b) were tested.

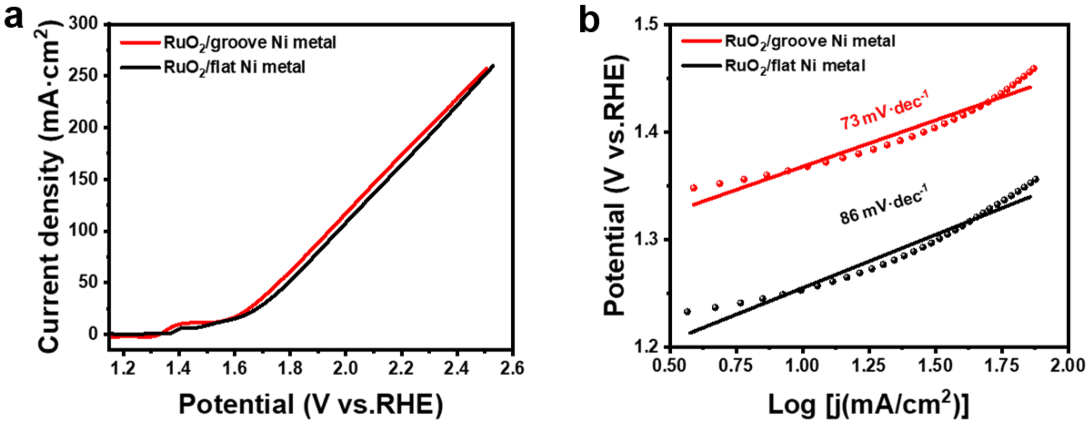

Fig. S16 (a) OER LSV curve of RuO_2 on groove Ni metal (η_{10} = 250 mV) and flat Ni metal (η_{10} = 286 mV). (b) Corresponding OER Tafel diagram.

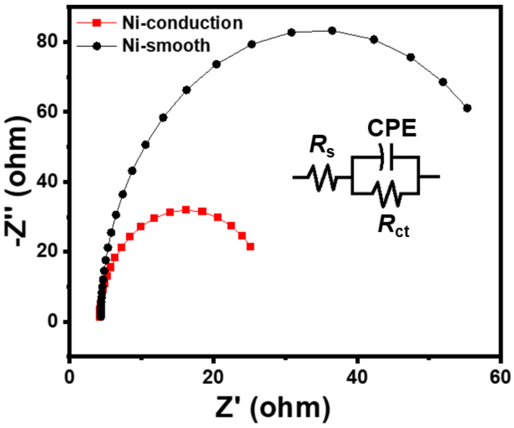

Fig. S17 Corresponding AC impedance spectra of Ni-conduction and Ni-smooth electrodes.

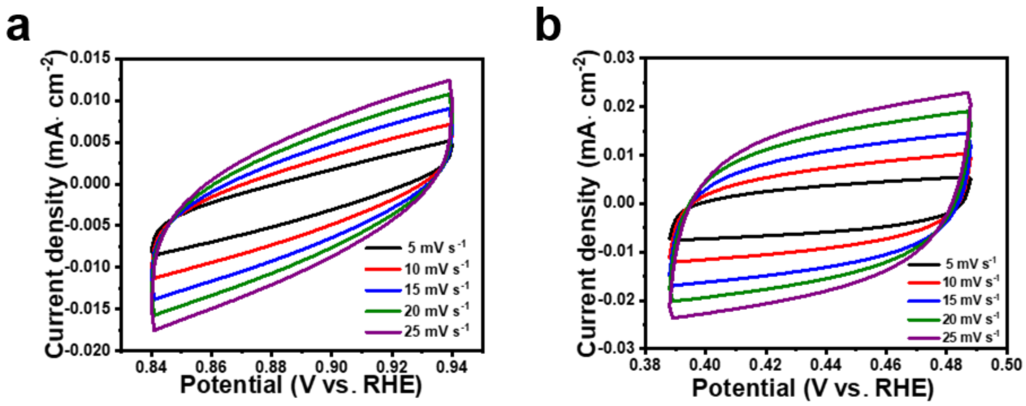

Fig. S18 Ni-conduction (a) and Ni-smooth (b) at different scan rates range from 5 to 25 mV·s^{-1} in 1.0 M KOH.

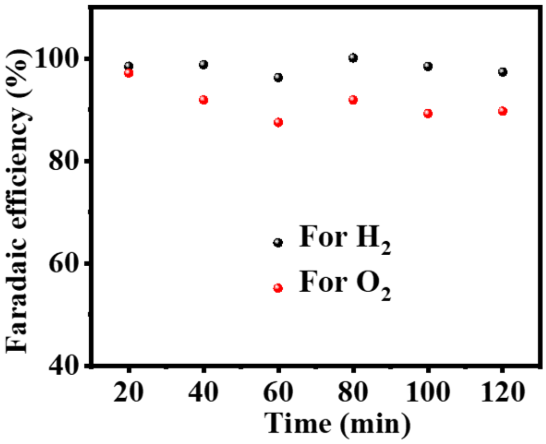

Fig. S19 Faradaic efficiencies of prepared Ni-conduction for in 1.0 M KOH.

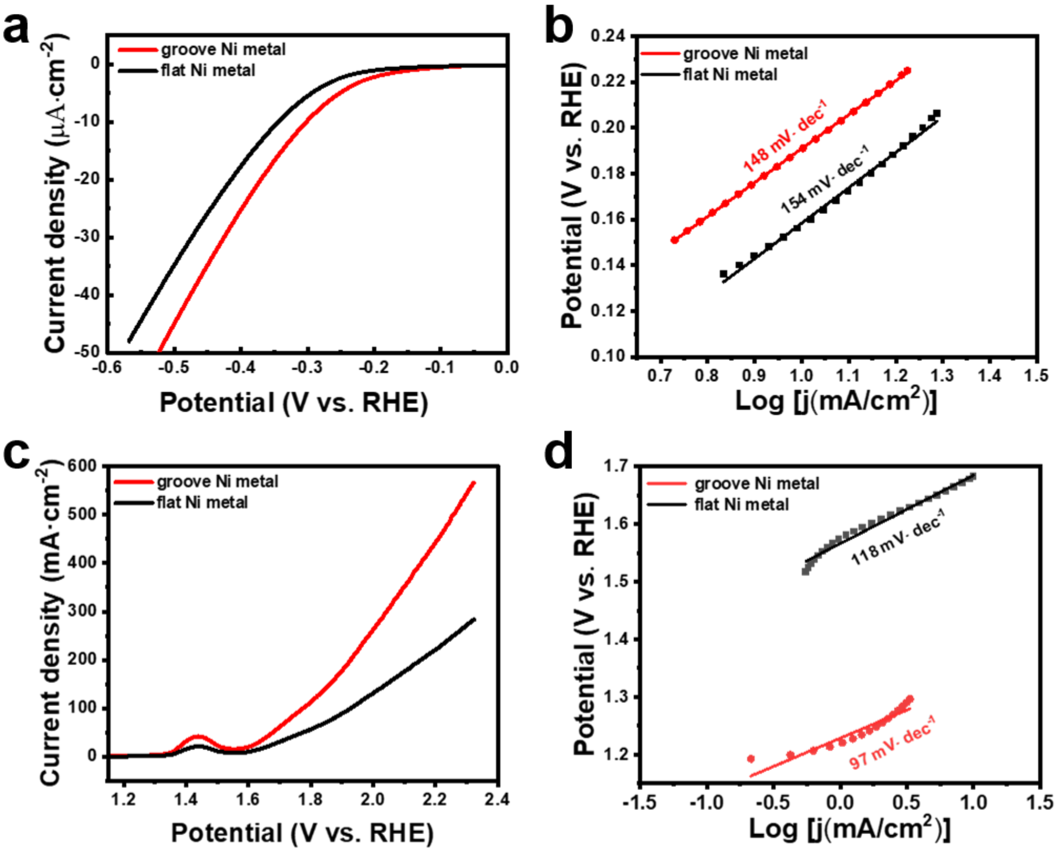

Fig. S20 HER LSV curve (a) of groove Ni metal (η_{10} = 302 mV) and flat Ni metal (η_{10} = 319 mV) without electrodeposition and the corresponding Tafel slope (b). OER LSV curve of groove Ni metal (η_{20} = 369 mV) and flat Ni metal (η_{20} = 427 mV) without electrodeposition (c) and the corresponding Tafel slope (d).

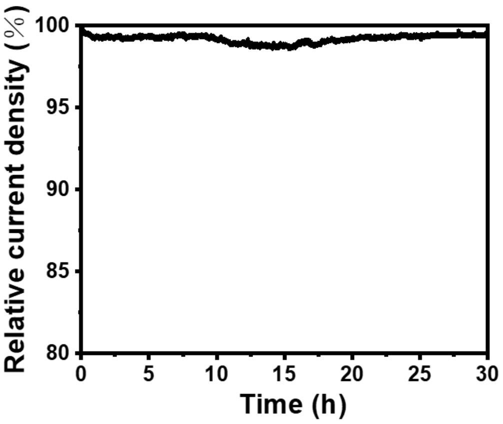

Fig. S21 The galvanostatic test of overall water splitting at 10 mA·cm^{-2}.

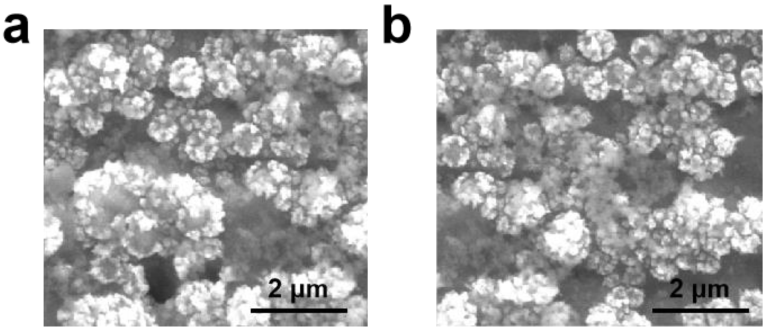

Fig. S22 SEM images of Ni-conduction after OER (a) and HER (b) 30 h stability test.

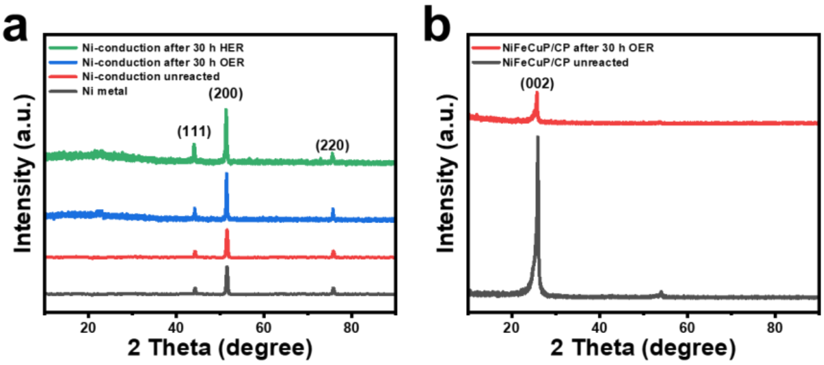

Fig. S23 (a) XRD pattern of Ni-conduction after HER and OER 30 h stability test. (b) XRD pattern of NiFeCuP/CP after OER 30 h stability test.

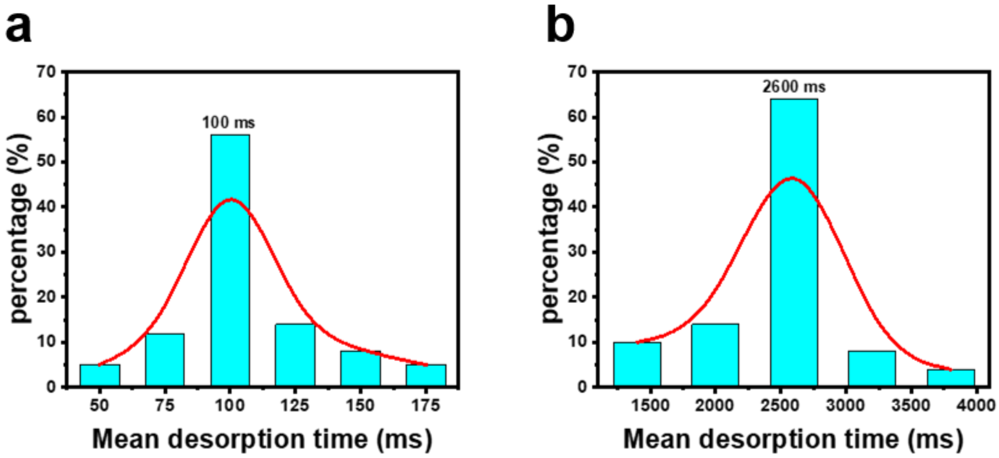

Fig. S24 Average desorption time statistics of bubbles for Ni-conduction (a) and Ni-smooth (b).

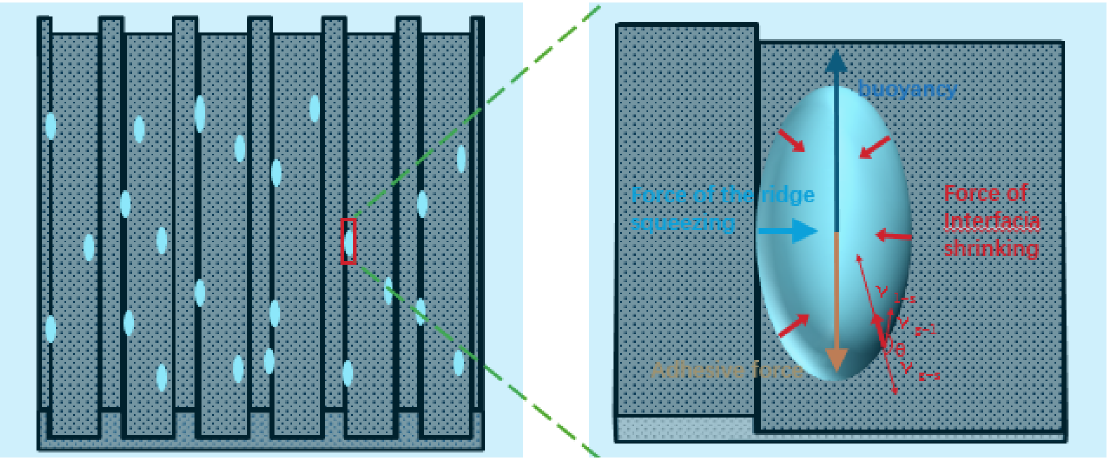

Fig. S25 Conducting force analysis of ellipsoid bubble nucleation in Ni-conduction.

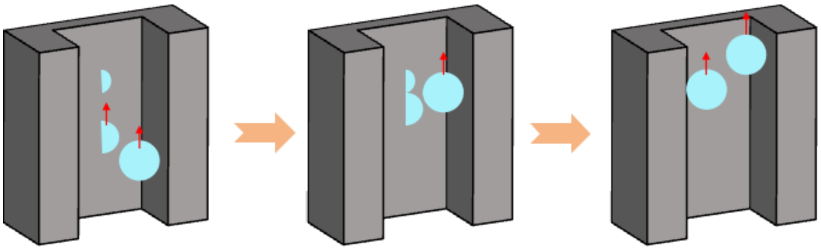

Fig. S26 The formation process of Ni-conducted bubble group.

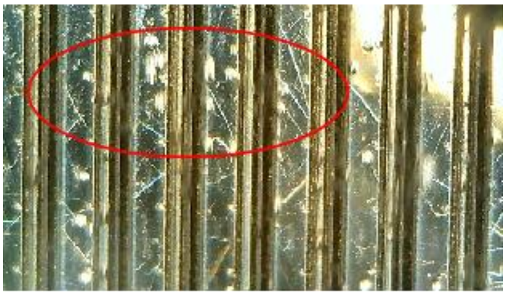

Fig. S27 Optical photograph of Ni-conducted bubble group.

Table S1. Based on the desorption angle in **Fig. 2f, Fig. 2h,** and **Fig. S13**, calculate the F_{ACH} of the bubble in Ni-conduction and Ni-smoothing.

	Angle of receding (°)	Angle of advance (°)	Contact line length (cm)	F_{ACH} (N)	Angle required for desorption (°)	Forward force of the bubble at 8°
Ni-conduction-X	98.1	125.2	0.58	$18.2 \cdot 10^{-5}$	24	$6.82 \cdot 10^{-5}$
Ni-conduction-Y	110.8	138.1	0.35	$6.6 \cdot 10^{-5}$	8	$6.82 \cdot 10^{-5}$
Ni-smooth-X	96.2	142.1	0.52	$25.5 \cdot 10^{-5}$	32	$6.82 \cdot 10^{-5}$
Ni-smooth-Y	96.2	142.1	0.52	$25.5 \cdot 10^{-5}$	32	$6.82 \cdot 10^{-5}$

Table S2. Comparison of the electrocatalytic activities of Ni-conduction with other recently reported electrocatalysts for OER, HER and overall water splitting potential in 1.0 M KOH.

Sample	HER overpotential@ j_{10}/mV	OER overpotential@ j_{10}/mV	Overall water splitting potential@ j_{10}/V	References
Ni–BTC/CC	441	390	-	[6]
Cu–BTC/CC	565	520	-	
Co–BTC/CC	437	370	2.02	
$CuFe_{0.6}S_{1.6}$	237	302	1.8	[7]
NiFe	270	300	-	.[8]
NiCo	210	360	-	
MoO_3/AC	353	280	-	[9]
MoO_3	387	350	-	
O-doped Co_2P/CuO nanowires (NWs)/CF	101	270	1.54	[10]
FeCo-N-C	-	380	-	[11]
Co-P/HNCW-800-300	-	287	1.55	[12]
CoFe10%-P/NF	68	227	1.61	[13]
1%C_{60} $(en)_n$-CoP-Co_2P	117	-	-	[14]
R-CoP_x/rGO(O)	-	268	-	[15]
P-3	-	126	-	[16]
Ni-conduction	92	123	1.53	**This Work**

References

1. W. Liu, X. Ding, J. Cheng, J. Jing, T. Li, X. Huang, P. Xie, X. Lin, H. Ding, Y. Kuang, D. Zhou and X. Sun, *Angew. Chem., Int. Ed.*, 2024, **63**, e202406082.
2. J. Kang, G. Liu, Q. Hu, Y. Huang, L.-M. Liu, L. Dong, G. Teobaldi and L. Guo, *J. Am. Chem. Soc.*, 2023, **145**, 25143-25149.
3. H. Li, S. Chen, Y. Zhang, Q. Zhang, X. Jia, Q. Zhang, L. Gu, X. Sun, L. Song and X. Wang, *Nat. Commun.*, 2018, **9**, 2452.
4. X. Zhao, P. Pachfule, S. Li, J. R. J. Simke, J. Schmidt and A. Thomas, *Angew. Chem., Int. Ed.*, 2018, **57**, 8921-8926.
5. C. Yu, X. Zhu, K. Li, M. Cao and L. Jiang, *Adv. Funct. Mater.*, 2017, **27**, 1701605.
6. S. Naik Shreyanka, J. Theerthagiri, S. J. Lee, Y. Yu and M. Y. Choi, *Chem. Eng. J.*, 2022, **446**, 137045.
7. X. Li, N. Ye, H. Liu, C. Li, Y. Huang, X. Zhu, H. Feng, J. Lin, L. Huang, J. Wu, Y. Liu, C. Liang and X. Peng, *Int. J. Hydrogen Energy*, 2022, **47**, 16719-16728.
8. J. Tourneur, L. Joanny, L. Perrin, S. Paul and B. Fabre, *ACS Appl. Eng. Mater.*, 2023, **1**, 2676-2684.
9. S. Sekar, J.-S. Yun, S. Park, D. Y. Kim, Y. Lee and S. Lee, *Int. J. Energy Res.*, 2024, **2024**, 3167699.
10. T. L. Luyen Doan, D. T. Tran, D. C. Nguyen, H. Tuan Le, N. H. Kim and J. H. Lee, *Appl. Catal., B*, 2020, **261**, 118268.
11. X.-G. Wu, R. Wang, F. Ma, X.-L. Liu, D.-L. Jia, H.-C. Yang, Y.-P. Liu, Z.-X. Wang, H.-Z. Zheng, Y.-N. Zhang, J. Hou, J.-J. Huang and S.-L. Peng, *Rare Met.*, 2023, **42**, 1526-1534.
12. W. Zhu, W. Hu, Y. Wei, Y. Zhang, K. Pan, S. Zhang, X. Hang, M. Zheng and H. Pang, *Adv. Funct. Mater.*, 2024, 2409390.
13. B. Liu, S. Li, T. Wang, Y. Yang, L. Wang, X. Zhang, Z. Liu and L. Niu, *Catal. Commun.*, 2023, **175**, 106607.
14. D. Yu, P. Guan, Y.-F. Huang, Y.-S. Cheng, M. Ling, K.-L. Wu, F.-H. Wu and X.-W. Wei, *Mater. Lett.*, 2023, **352**, 135184.
15. X. Zhou, H. Gao, Y. Wang, Z. Liu, J. Lin and Y. Ding, *J. Mater. Chem. A*, 2018, **6**, 14939-14948.
16. X. Q. Han, N. Lin, X. C. Zhang, W. J. Zhang, Z. Y. Wang and C. Ma, *J. Alloys Compd.*, 2023, **947**, 169603.